# scientific reports



## **OPEN** Seismic performance of multistory frames with novel self-centering friction SMA dampers

Weihong Li<sup>1</sup>, Zhaogun Chang<sup>2⊠</sup>, Meng Han<sup>2</sup>, Jinyuan Li<sup>2</sup>, Qinkai Jin<sup>2</sup> & Boguan Liu<sup>2</sup>

Owing to their advantageous properties of super-elasticity and shape memory effect, shape memory alloys (SMAs) can dissipate seismic energy and minimize post-earthquake structural damage. In this study, an improved SMA multi-linear constitutive model is proposed first, and a new material model based on OpenSees platform is developed. Secondly, a new self-centering friction damper (SCFD) is proposed by combining SMA and friction material, and a numerical model is established and validated by damper tests. Finally, detailed finite element models of RC frames equipped with SCFDs, bucklingrestrained braces, and self-centering dampers are established. Peak and residual inter-story drift ratio of different cases are analyzed, and seismic control effectiveness of different energy dissipation devices is compared through comprehensive evaluation indices. The results show that the improved SMA multi-linear constitutive model can accurately characterize its hysteresis response. The SCFD reduces the residual inter-story drift ratio to below 0.1% under rare earthquakes and decreases the peak interstory drift ratio by 43.5% compared to uncontrolled structures under extremely rare earthquakes, and structural function recovery can be achieved.

**Keywords** Shape memory alloy, Constitutive model, Self-centering damper, Experimental test, Seismic control, Dynamic analysis

Energy-dissipation devices provide the advantages of simple construction and excellent damping effects and are universally used in practical engineering. They can effectively reduce structural response under seismic loads and satisfy the goal of structural vibration control<sup>1-3</sup>. To this end, various types of seismic energy-dissipating devices<sup>4–7</sup> have been developed. Friction dampers<sup>8</sup> feature simple construction, low cost, and robust energydissipation capacity, yet they remain inactive under small displacements and induce notable additional stiffness. Metallic dampers<sup>9-11</sup>exhibit superior low-cycle fatigue resistance, stable hysteresis behavior, and temperature insensitivity, but necessitate replacement after yielding. Viscoelastic dampers<sup>12,13</sup> possess strong energy-dissipation capability but demonstrate high sensitivity to temperature and frequency fluctuations, accompanied by long-term stiffness degradation. Viscous dampers achieve high energy-dissipation efficiency without introducing structural stiffness, though they are susceptible to viscous fluid leakage and entail intricate maintenance. Owing to their unique shape-memory effect and super-elastic performance, shape-memory alloys (SMAs) have become the subject of increasing interest 14,15. Moreover, dampers made of SMA materials provide the advantages of large recoverable deformation and fatigue resistance.

Previous research on SMAs has predominantly concentrated on seismic applications, including SMA dampers<sup>16-25</sup> and vibration isolation systems<sup>26,27</sup>. More recently, SMA hybrid dampers have been developed to boost energy dissipation. For example, Qian et al.<sup>17</sup> introduced a novel superelastic SMA friction damper that utilizes pre-tensioned SMA elements to improve re-centering while its friction components deliver significant energy dissipation. Similarly, Naeem et al.<sup>28</sup> designed a hybrid energy-dissipation device that integrates an SMA bar for re-centering with a steel slit plate to enhance energy dissipation. In addition, Liu et al.<sup>29</sup> proposed an innovative self-centering negative-stiffness damper that combines SMA with precompressed springs, with simulation results indicating that the inclusion of negative stiffness substantially increases the damping ratio.

To better apply SMAs in practical engineering applications, a constitutive model that can accurately describe their mechanical characteristics is required. Currently, three theoretical models for SMAs exist based on different theoretical foundations: mesoscopic thermodynamic, mesoscopic mechanical, and macroscopic phenomenological models. Generally, mesoscopic thermodynamic models include Ortin-Planes, Berveiller, and Ferdinando models<sup>30–32</sup>. Mesoscopic mechanical models include Sun-Hwang and Boyd-Lagouds models<sup>33–35</sup>. Both model types are based on the thermodynamic theory, and the mechanical properties of SMAs are explained

<sup>1</sup>School of Management, Xi'an University of Finance and Economics, Xi'an 710100, China. <sup>2</sup>School of Civil Engineering, Chang'an University, Xi'an 710061, China. <sup>™</sup>email: czq199212@163.com

from a microscopic perspective. However, they are rarely applied in practical engineering because of their complexity.

Macroscopic phenomenological models are primarily based on experimental results and can be used to describe the macroscopic mechanical behavior of SMAs. Some commonly used models include the Tanake, Liang–Roger, and Brinson models<sup>36–39</sup>. Özdemir<sup>40</sup> proposed a constitutive model with plastic mechanical characteristics, and Graesser et al.<sup>41,42</sup> further improved this model. Li et al.<sup>43</sup> conducted a series of tests on SMA wires, and proposed a multi-linear dynamic constitutive model considering multiple factors. To investigate the damping effect of SMA-based dampers in structures by finite-element analysis, constitutive models must be provided on various nonlinear analysis software platforms for researchers to choose from. Currently, the OpenSees platform is commonly used for nonlinear analysis under seismic conditions. However, the constitutive model of the Self-Centering material in its built-in material library cannot accurately describe the mechanical behavior of the SMA. Therefore, the constitutive model needs to be improved.

In this study, an improved multi-linear constitutive model for SMA is proposed, which comprehensively considers factors such as residual deformation and stress degradation at the start of the martensitic transformation. Second, deep development is conducted for the improved constitutive model using the OpenSees platform. Furthermore, the newly defined material model is applied to a novel self-centering friction damper (SCFD). Finally, the damping-control effects of different types of displacement-based dampers are compared and analyzed by analyzing the structural responses, such as the peak displacement and residual inter-story drift ratio.

### Improved SMA constitutive model development Improved SMA constitutive model

To describe the super-elastic characteristics of SMAs, Lagoudas et al.<sup>44</sup> assumed that each stage of the stress-strain curve exhibited a linear relationship, and a simplified multi-linear constitutive model was proposed. This model is relatively simple in form and computationally efficient, but some aspects are not considered: (i) the residual deformation of SMAs, (ii) the degradation phenomenon of the initial stress of the martensite phase transformation, and (iii) the difference between the loading and unloading paths during martensite hardening.

As shown in Fig. 1, an improved SMA constitutive model is proposed.  $\sigma_{\rm Ms}$  and  $\varepsilon_{\rm Ms}$  represent the initiation stress and corresponding strain for the forward transformation (austenite to martensite), respectively;  $\sigma_{\rm Mf}$  and  $\varepsilon_{\rm Mf}$  denote the completion stress and corresponding strain for the forward transformation (austenite to martensite), respectively;  $\sigma_{\rm As}$  and  $\varepsilon_{\rm As}$  represent the initiation stress and corresponding strain for the reverse transformation (martensite to austenite), respectively;  $\sigma_{\rm Af}$  and  $\varepsilon_{\rm Af}$  denote the completion stress and corresponding strain for the reverse transformation (martensite to austenite), respectively;  $k_1$  and  $k_3$  are the elastic deformation modulus in the austenite state and martensite state during the loading stages, respectively; and  $k_2$  is the loading modulus in the martensite transformation state (austenite to martensite).

Based on previous tests on SMAs<sup>45</sup>, the hysteresis characteristics are closely related to the maximum historical strain. Therefore, the hysteresis curve was divided into three stages based on the maximum strain: (i) the elastic, (ii) phase-transformation, and (iii) transformation-hardening stages. The mechanical behaviors of each stage are described as follows:

(i) Elastic stage ( $\varepsilon < \varepsilon_{Ms}$ )

$$\sigma = k_1(\varepsilon - \varepsilon_r) \quad (E \leftrightarrow A) \tag{1}$$

(ii) Phase transformation stage  $(\varepsilon_{Ms} \le \varepsilon < \varepsilon_{Mf})$ .

When the maximum strain during loading does not exceed  $\varepsilon_{MP}$  the complete phase-transformation path is *OE-ABCDE*. If it exceeds  $\varepsilon_{MP}$  then the path is *OEABCD'E'*, and the residual strain increases, resulting in a degra-

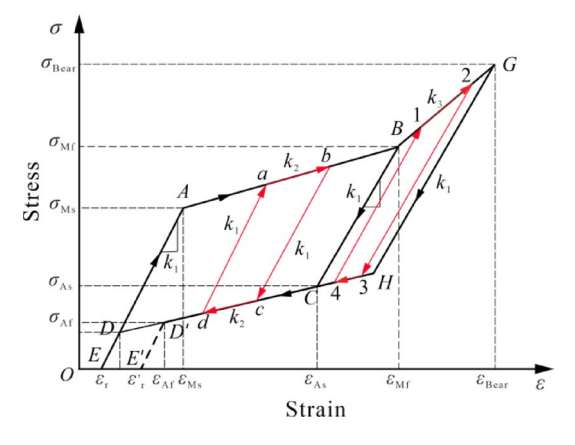


Fig. 1. Modified SMA constitutive model.

dation of the stress level when the martensite phase transformation starts during the next loading. Therefore, the stress–strain relationship can be described as follows:

$$\sigma = \begin{cases} \sigma_{\text{Ms}} + k_2(\varepsilon - \varepsilon_{\text{Ms}}), & (A \to B) \\ \sigma_{\text{Mf}} + k_1(\varepsilon - \varepsilon_{\text{Mf}}), & (B \to C) \\ \sigma_{\text{As}} + k_2(\varepsilon - \varepsilon_{\text{As}}), & (C \to D/Dt) \\ \sigma_{\text{Af}}(\sigma t_{\text{Af}}) + k_1(\varepsilon - \varepsilon_{\text{r}}(\varepsilon t_{\text{r}})), & (D/Dt \to E/Et) \end{cases}$$
(2)

During the loading process, if unloaded at point B, and the strain after unloading is less than  $\varepsilon_{AP}$  then the hysteresis path is a-b-c-d-a, that is:

$$\sigma = \begin{cases} \sigma_{\rm b} + k_1(\varepsilon - \varepsilon_{\rm b}), & (b \to c) \\ \sigma_{\rm c} + k_2(\varepsilon - \varepsilon_{\rm c}), & (c \to d) \\ \sigma_{\rm d} + k_1(\varepsilon - \varepsilon_{\rm d}), & (d \to a) \\ \sigma_{\rm a} + k_2(\varepsilon - \varepsilon_{\rm a}), & (a \to b) \end{cases}$$
(3)

### (iii) Transformation-hardening stage ( $\varepsilon \ge \varepsilon_{Mf}$ ).

Assuming that the stiffness remains constant during the unloading process of the transformation-hardening stage, the mechanical behavior of the SMA can be described as follows:

$$\sigma = \begin{cases} \sigma_{\mathrm{Mf}} + k_{3}(\varepsilon - \varepsilon_{\mathrm{Mf}}), & (B \to G) \\ \sigma_{\mathrm{Bear}} + k_{1}(\varepsilon - \varepsilon_{\mathrm{Bear}}), & (G \to H) \\ \sigma_{\mathrm{H}} + k_{2}(\varepsilon - \varepsilon_{\mathrm{H}}), & (H \to C) \end{cases}$$
(4)

The hysteresis subloop exhibits the same behavior as the phase transformation stage, and the path is 2-3-4-1-2:

$$\sigma = \begin{cases} \sigma_2 + k_2(\varepsilon - \varepsilon_2), & (2 \to 3) \\ \sigma_3 + k_2(\varepsilon - \varepsilon_3), & (3 \to 4) \\ \sigma_4 + k_1(\varepsilon - \varepsilon_4), & (4 \to 1) \\ \sigma_1 + k_3(\varepsilon - \varepsilon_1), & (1 \to 2) \end{cases}$$
 (5)

In the proposed improved model, the parameters  $k_1, k_2, k_3, \sigma_{\rm Ms}, \varepsilon_{\rm Mf}, \varepsilon_{\rm r}$ , and  $\varepsilon_{\rm As}$  can be obtained from experimental results. The mathematical relationship between  $\sigma_{\rm Ms}$ ,  $\varepsilon_{\rm r}$  and the maximum historical strain can be determined through numerical fitting.

#### Model development and validation

The proposed SMA constitutive model was developed using the OpenSees platform. This process can be summarized as follows.

Step 1 Writing the head file. In this file, we create the Damper\_SMA class and then declare the necessary member functions and member variables. Member-variable permissions must also be considered.

Step 2 Establishing the source file. The source file contains the head file from the previous step, and the member functions in the head file are conducted. Among them, the setTrialStrain function is the most important because it determines the stress–strain relationship of a material. A flowchart of the setTrialstrain function in the source file is shown in Fig. 2.

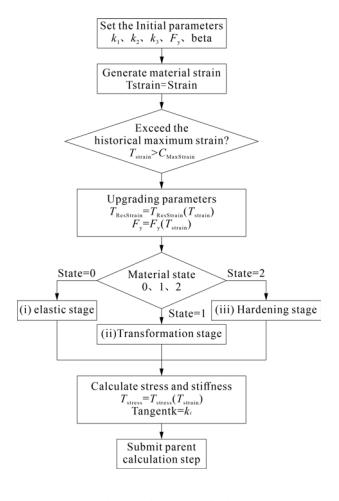


Fig. 2. Flowchart of the setTrialStrain function.

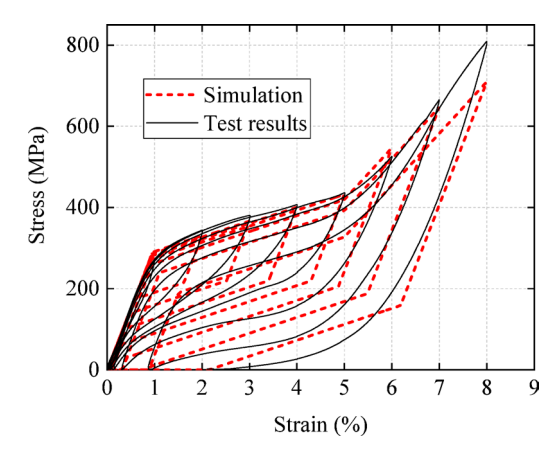


Fig. 3. Comparison of model prediction with cyclic test results.

Strain (%)	Data type	Energy dissipation per cycle W(J)	Equivalent damping ratio $\xi_{\rm eq}$	Equivalent stiffness K(kN/mm)
	Simulation	10.06	0.0482	1.06
4	Test results	11.86	0.0487	1.08
	Error	-2.70%	-1.13%	-1.59%
	Simulation	18.52	0.0560	0.92
5	Test results	19.03	0.0512	0.93
	Error	8.51%	9.49%	-0.9%
	Simulation	29.07	0.0495	0.97
6	Test results	26.79	0.0512	0.93
	Error	-6.84%	-3.32%	3.95%
	Simulation	38.95	0.0451	0.98
7	Test results	38.76	0.0471	1.01
	Error	-9.55%	-4.24%	-2.72%

Table 1. Comparison results at various strain amplitudes.

Step 3 Compilation. The prepared file is compiled to generate a dynamic link library file and the file is placed in the same folder as the OpenSees main program. Finally, the codes are debugged and compared with the test results to verify the effectiveness of the model.

After compiling, a two-dimensional single-degree-of-freedom model of the SMA was established using the  $\mathit{Tcl}$  language command. A comparison between the simulation results and experimental data is presented in Fig. 3<sup>45</sup>. Three key parameters, namely the energy dissipation per cycle  $\mathit{W}$ , equivalent viscous damping ratio  $\xi_{\rm eq}$ , and equivalent stiffness  $\mathit{K}$ , were selected to analyze the simulation results, as summarized in Table 1. The  $\mathit{K}$  value is calculated as the ratio of the peak stress  $\sigma_{\rm max}$  to the maximum strain  $\varepsilon_{\rm max}$  at that cycle.  $\mathit{W}$  denotes the area surrounded by the curve with a single loading cycle.  $\xi_{\rm eq}$  can be calculated as follows:

$$\xi_{\rm eq} = \frac{W}{2\pi K D_{\rm max}^2} \tag{6}$$

The results indicate that the newly defined material can accurately simulate the hysteretic behavior of the SMA. The various indicators were in good agreement with the experimental results.

#### Self-centering friction damper Experimental tests of the SCFD

As illustrated in Fig. 4<sup>46</sup>, the self-centering friction damper (SCFD) consists of both a self-centering mechanism and a friction module. Under external loads, deformation occurs between the inner and outer steel plates, allowing the friction component to dissipate energy. Simultaneously, the SMA bars extend when the SCFD is subjected to either tensile or compressive forces. Together, these devices not only dissipate energy but also enable the damper to return to its original configuration after loading. The damper's operating principle is detailed in 45.

Based on the optimal results of a previous study, a large-scale prototype of SCFD of 1310 mm was fabricated and tested. The self-centering and friction devices of SCFD were individually tested first, and results are shown in Fig. 5a. The hysteretic curves of the SCFD are shown in Fig. 5b<sup>48</sup>. Results indicate that the SCFD exhibited symmetrical behavior and excellent energy dissipation and self-centering. Notably, the hysteretic curve of the

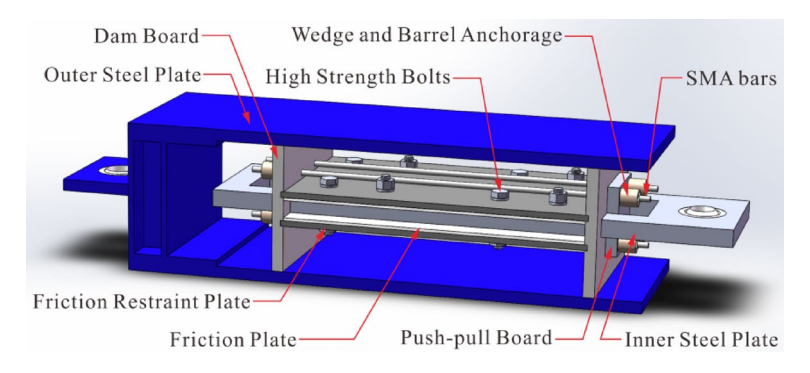
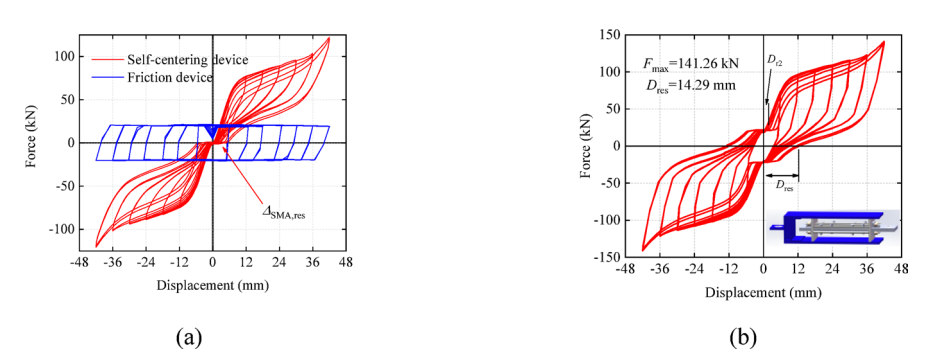
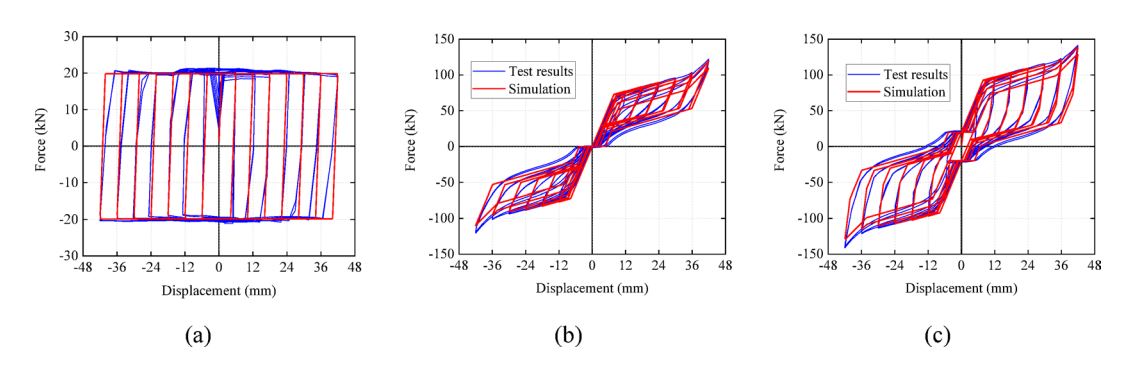


Fig. 4. 3D schematic representation of SCFD, modeled by SolidWorks Premium 2020 SP $0.0^{47}$  (original artwork by the author).



**Fig. 5**. Cyclic behavior: (a) SCFD components; (b) the SCFD.



**Fig. 6.** Comparison of experimental and numerical results: (a) Friction device; (b) self-centering device; (c) SCFD.

damper did not have an obvious yield point. This phenomenon can be explained as follows: strand-tapered anchorage was used to fix two ends of each SMA bar, and this anchorage configuration causes an inevitable minor drift when the SCFD experiences external cyclic loads, resulting in non-synchronization of the deformation development of SMAs. Thus, the SMA bars failed to yield simultaneously.

#### Validation of numerical model

Based on the OpenSees platform, a finite element model of the SCFD has been developed. In this model, the friction device is simulated with the Steel01 material, while the SMA component for the self-centering mechanism (Damper\_SMA) is modeled using the improved constitutive formulation described in "Model development and validation" section. These two materials are arranged in parallel via the Parallel command. Figure  $6^{48}$  illustrates the hysteretic responses of both the numerical and experimental models. To assess simulation accuracy, three key parameters were calculated and compiled as shown in Table 2, with errors maintained within 9.0%. The close agreement between the numerical and experimental force—displacement curves confirms that the model can be reliably used for further analysis.

Displacement	W (k)	I)		ξ <sub>eq</sub> (%)			K (kN/mm)			
amplitude	Test	Simulation	Error (%)	Test	Simulation	Error (%)	Test	Simulation	Error (%)	
12	1.24	1.20	-2.75	17.40	16.39	-5.82	7.85	8.11	3.26	
-12	1.27	1.20	-5.32	17.56	16.44	-6.34	7.99	8.08	1.09	
18	2.16	2.14	-1.12	18.79	18.27	-2.76	5.66	5.75	1.69	
-18	2.20	2.07	-6.14	18.93	17.78	-6.07	5.71	5.71	-0.07	
24	3.23	3.01	-6.81	19.62	18.24	-7.05	4.55	4.56	0.26	
-24	3.21	2.98	-7.19	19.49	18.36	-5.79	4.55	4.49	-1.48	
30	4.13	3.91	-5.25	18.92	18.17	-3.96	3.86	3.81	-1.34	
-30	4.05	3.82	-5.71	18.78	18.35	-2.31	3.81	3.68	-3.48	
36	5.08	4.69	-7.63	18.26	16.98	-6.99	3.42	3.39	-0.70	
-36	4.90	4.48	-8.43	17.82	17.13	-3.90	3.37	3.21	-4.71	
42	5.68	5.36	-5.70	15.24	14.58	-4.33	3.36	3.32	-1.43	
-42	5.44	5.00	-8.07	14.77	14.59	-1.23	3.32	3.09	-6.92	

Table 2. Comparison results of test and simulation models.

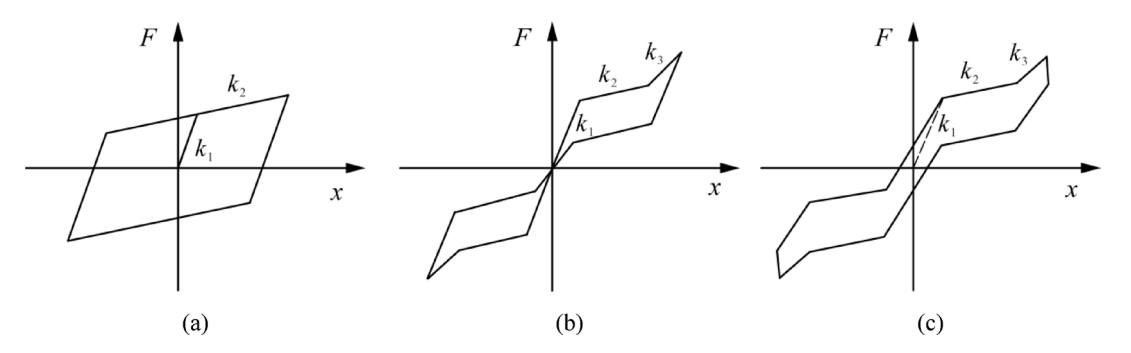


Fig. 7. Constitutive models of three energy-dissipating devices: (a) buckling restrained brace; (b) self-centering device; (c) SCFD.

#### Investigation of seismic effect of different energy-dissipating devices

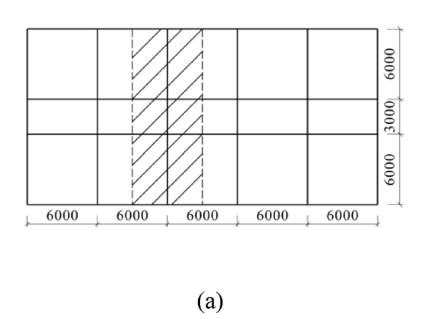
To investigate the seismic effect of SCFDs, three different displacement-type energy-dissipating devices are selected to analyze the structural response in terms of the maximum inter-story drift ratio, residual inter-story drift ratio, and peak acceleration. The three types of energy-dissipating devices are illustrated in Fig. 7. SCFD is a multilinear hysteresis model. The buckling-restrained brace (BRB) and self-centering device are bilinear and flag-type hysteresis models, respectively. These three devices have an initial stiffness and a secondary stiffness that can dissipate the seismic-energy input into the structure by deformation.

#### Overview of the structural modeling

Based on China's Code for Seismic Design of Buildings (GB 50,011)<sup>49</sup>, an 11-story reinforced concrete (RC) frame structure was modeled using the PKPM software<sup>50</sup>. The analytical model was designed based on a reinforced concrete multi-tower high-rise building with a large podium located in an intensity Degree VIII earthquake zone per the Chinese Code, featuring a basic acceleration of 0.2g at a Group III, Class II seismic site. Standard live load values of 2.0, 2.5, and 0.5 kN/m² are applied for floors, corridors, and unoccupied roofs, respectively. The first floor is 4.2 m high, each subsequent floor is 3.6 m, and the building reaches a total height of 40.2 m. The shaded portion of the frame depicted in Fig. 8 represents the analytical model used in this section. Table 3 outlines design details such as beam and column dimensions, concrete strength, and reinforcement type, while Table 4 presents the reinforcement specifications derived from the PKPM design program.

Concrete02 is used for the concrete constitutive model, Steel02 is used for the steel reinforcement constitutive model, the fiber model is used for the cross-section analysis model of the members, and the nonlinear beam-column unit model is developed using the stiffness method. To ensure the accuracy of the nonlinear analysis and obtain a refined model, each beam or column is divided into three segments, which are used to reflect the influence of the local reinforcement zone on the structural response. The damping ratio is 0.05 and the P- $\Delta$  effect is considered in the analysis process.

Energy-dissipating devices are installed on the structure by fixing the two ends to the adjacent floors on each story of the frame, as shown in Fig. 7b. The bracing supports connected to the dampers are simulated with an elastic material and assigned high stiffness. To simplify the calculation, only the core unit is selected as the support for the BRBs, and the Steel02 material is used for the simulation. The SCFD is simulated using the newly



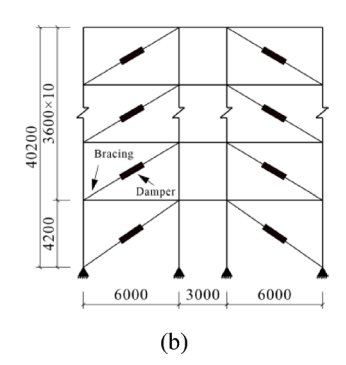


Fig. 8. Description of the test frame model: (a) frame plan; (b) frame elevation.

Design parameters	Value
Beam section (mm)	500×300
Column section (mm)	1–6 floor: 00×600; 7–11 floor: 550×550
Concrete strength	Grade 35
Longitudinal steel bars	HRB400
Steel stirrups	HPB300
Diameter of steel stirrups (mm)	8
Local zone reinforcement of steel stirrups (mm)	100
General spacing of steel stirrups (mm)	200

Table 3. Design parameters of test RC frame.

	Column		Beam				
Floor	Side column   Middle column		Side-span (Top + Bottom)	Mid-span (Top + Bottom)			
1	4Ф25	4Φ25	4Φ25+4Φ16	4Φ25+4Φ25			
2	4Ф25	4Φ25	4Φ25 + 4Φ16	4Φ25+4Φ25			
3	4Ф25	4Φ25	4Φ25 + 4Φ16	4Φ25+4Φ25			
4	4Ф22	4Φ22	4Φ25+4Φ16	4Φ25+4Φ25			
5	4Ф22	4Φ22	4Φ22+4Φ16	4Φ22+4Φ20			
6	4Ф22	4Φ22	4Φ22+4Φ16	4Φ22+4Φ20			
7	4Ф22	4Φ22	4Φ22+4Φ16	4Φ22+4Φ18			
8	4Ф22	4Φ22	4Φ22+4Φ16	4Φ22+4Φ18			
9	4Ф22	4Φ22	4Φ22+4Φ16	4Φ22+4Φ16			
10	4Ф22	4Φ22	4Φ22+4Φ16	4Φ22+4Φ16			
11	4Φ22	4Ф22	4Φ20+4Φ16	4Φ22+4Φ16			

Table 4. Reinforcement parameters of RC frame columns and beams.

developed SMA material described in Sect. 3.3. The initial equivalent stiffness  $K_1$  of the three devices is 30 kN/mm.

#### Model validation

To verify the effectiveness of the selected materials and members, BRBs in the literature<sup>51</sup> are selected for the finite-element simulation, and the BRB core material is selected as Steel02 Material. Figure 9a and b shows a comparison of the experimental and numerical results for specimens W-5 and W-6. The results show that the method can simulate the hysteresis characteristics of BRBs with relative accuracy. Moreover, a 1/2 scaled RC frame from the literature<sup>52</sup> is also selected for verification, the steel and concrete materials are respectively selected as Steel02 and Concrete02, using fiber cross-sections, the element selects dispBeamColumn, and each beam and column is divided into three elements, as shown in Fig. 9c. The numerical curves are in good agreement with the test results, which verified the accuracy of the finite-element model.

#### Earthquake ground motions

In this study, the target response spectrum is defined according to the seismic design code for buildings. Five recorded earthquake ground motions were selected from the PEER database, and two synthetic seismic

**Fig. 9.** Comparison of experimental and numerical results: (a) Specimen W-5; (b) Specimen W-6; (c) RC frame.

Order	Name of the earthquake records	Year	Intensity	Time/s
1	Imperial Valley-06, El Centro Array #4	1979	6.53	10.3
2	Loma Prieta, Saratoga—Aloha Ave	1989	6.93	9.4
3	Landers, Amboy	1992	7.28	28.5
4	Chi-Chi_ Taiwan, TCU053	1999	7.62	27.7
5	Cape Mendocino, Centerville Beach_ Naval Fac	1992	7.01	10.6

Table 5. Five ground motions used in the analysis.

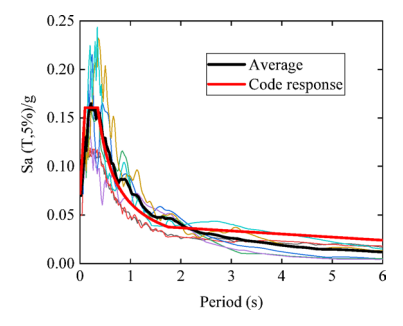


Fig. 10. Acceleration spectra of individual ground motions.

waves were generated, resulting in a total of seven seismic records for time–history analysis. The details and corresponding response spectra are provided in Table 5 and Fig. 10. The peak accelerations (PAs) of ground motions for frequent, basic, major, and extremely strong earthquakes are 0.07 g, 0.20 g, 0.40 g, and 0.60 g, respectively. The probability of exceedance over 50-year period (FPOE) for the first three earthquake intensities are 10%, 63%, and 2%, respectively. In each case, the structure was allowed to vibrate freely for 30 s after the earthquake excitation ended.

#### Structural seismic responses and discussion

To avoid the influence of specific ground motions on the analysis results for a specific structure, the average value of the structural response under seven seismic waves is selected as the basis for the analysis. To explicitly demonstrate the effectiveness of the seismic control, the reduction ratios are introduced as follows:

Reduction ratio = 
$$\left(1 - \frac{\text{Response of controlled structure}}{\text{Response of original structure}}\right) \times 100\%$$
 (7)

Figure 11 displays the peak inter-story drift ratios (PIDRs) for each story, while Table 6 summarizes the corresponding reduction ratios. In this context, NDF represents an uncontrolled structure, BRBF is a frame equipped with BRBs, SCDF features self-centering devices, and SCFDF includes SCFDs. As shown in Fig. 11, the maximum PIDR ( $\theta_{\rm max}$ ) in controlled structures is considerably lower than in the uncontrolled one, and SCFDF exhibits superior performance compared to BRBF and SCDF under both multiple-occurring and design-level earthquake scenarios. The friction component adds lateral stiffness, thereby diminishing the seismic response. In particular, during an extremely rare earthquake, the building collapses as the maximum PIDR exceeds the

Fig. 11. Structural peak inter-story drift ratio under seismic waves: (a) multi-occurring earthquake; (b) design earthquake; (c) rare earthquake; (d) extremely rare earthquake.

	NDF	F BRBF		SCDF		SCFDF	
Earthquake ground motion level	$\theta_{ m max}$	$\theta_{ m max}$	Reduction ratio (%)	$\theta_{ m max}$	Reduction ratio (%)	$\theta_{ m max}$	Reduction ratio (%)
Multiple-occurring	1/548	1/918	40.3	1/920	40.4	1/920	63.4
Design	1/174	1/292	40.7	1/300	42.2	1/393	55.9
Rare	1/67	1/130	48.6	1/120	44.2	1/143	53.1
Extremely rare	1/39	1/67	41.1	1/67	41.2	1/70	43.5

**Table 6**. Reduction ratio of PIDR  $\theta_{max}$ .

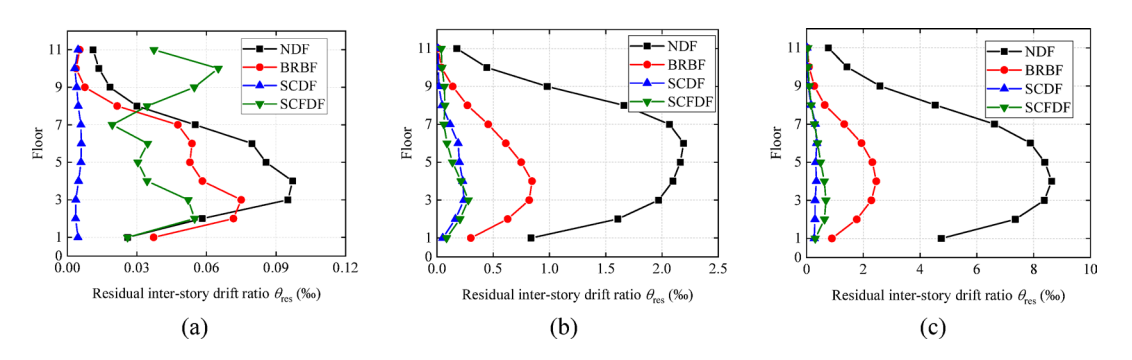


Fig. 12. Structural residual inter-story drift ratio under seismic waves: (a) design earthquake; (b) rare earthquake; (c) extremely rare earthquake.

	NDF	BRBF		SCDF		SCFDF	
Earthquake ground motion level	$\theta_{ m res}$	$\theta_{ m res}$	Reduction ratio (%)	$\theta_{ m res}$	Reduction ratio (%)	$\theta_{ m res}$	Reduction ratio (%)
Multiple-occurring	1/548	1/918	40.3	1/920	40.4	1/920	63.4
Design	1/174	1/292	40.7	1/300	42.2	1/393	55.9
Rare	1/67	1/130	48.6	1/120	44.2	1/143	53.1
Extremely rare	1/39	1/67	41.1	1/67	41.2	1/70	43.5

**Table 7.** Reduction ratio of RIDR  $\theta_{res}$ .

2.0% threshold permitted by the Chinese seismic design code<sup>48</sup>. Additionally, Table 6 reveals that the average reduction ratios for BRBF, SCDF, and SCFDF all surpass 40%.

The residual inter-story drift ratio (RIDR) is a key indicator of structural damage. According to FEMA P-58<sup>53</sup>, there are four IDR limit categories, with the DS1 class requiring a RIDR below 0.2%. Figure 12 presents the RIDRs for each floor, while Table 7 lists the associated reduction ratios. In uncontrolled structures, rare and extremely rare earthquakes can produce RIDR values exceeding 0.2% (but remaining below 0.5%), which, based on design guidelines<sup>53</sup>, permits economically feasible realignment and repairs with minimal impact on overall stability. In contrast, controlled structures consistently show RIDRs below 0.1%, indicating no need for repair; notably, the RIDRs for SCFDF and SCDF systems are lower than those for BRBF. These results underscore the significant effect of SMA materials. The restoring force of the SMAs drives the structure to self-center after seismic events, markedly reducing residual displacements. Under rare and extremely rare earthquake conditions, BRBs tend to

Earthquake ground motion level	BRBF	SCFD	SCFDF
Multiple-occurring	0.730	0.731	0.699
Design	0.711	0.701	0.560
Rare	0.607	0.581	0.515
Extremely rare	0.606	0.570	0.550

**Table 8**.  $\varphi$  results of each case (%).

yield, leaving a considerable residual displacement that necessitates replacement, whereas the super-elasticity of SMAs prevents large permanent deformations, eliminating the need for replacement.

#### Performance assessment function

Based on structural dynamic response analysis, the spatial distribution of local parameter extremes exhibits no deterministic correlation with the location of systematically weak stories in the structural system. The effects of each index should be considered for structural vibration control. Some studies<sup>54</sup> have suggested combining the PIDR, peak acceleration, and peak displacement as an objective function to measure the safety of the structure, which is introduced as follows:

$$p = \alpha \frac{\theta_{\text{max}}}{\theta_{0 \text{ max}} + \beta \frac{A_{\text{max}}}{A_{0 \text{ max}} + \gamma \frac{U_{\text{max}}}{U_{0 \text{ max}}}}}$$
(8)

where each quantity is the average value under the excitation of earthquake ground motions.  $\theta_{\max}$  and  $\theta_{0\max}$  are PIDRs of the controlled and uncontrolled structures, respectively.  $A_{\max}$  and  $A_{0\max}$  are the peak accelerations of the controlled and uncontrolled structures, respectively.  $U_{\max}$  and  $U_{0\max}$  are the peak displacements of the controlled and uncontrolled structures, respectively.  $\alpha$ ,  $\beta$ , and  $\gamma$  are coefficients.

In this study, Eq. (8) is modified by introducing the RIDRs of the structures and is given by:

$$\varphi = \alpha \frac{\theta_{\text{max}}}{\theta_{0 \text{ max}} + \beta \frac{A_{\text{max}}}{A_{0 \text{ max}} + \gamma \frac{U_{\text{max}}}{U_{0 \text{ max}} + \mu \frac{\theta_{\text{r}}}{\theta_{0 \text{r}}}}}$$
(9)

where  $\theta_r$  and  $\theta_{0r}$  are the RIDRs of the controlled and uncontrolled structures, respectively, and  $\mu$  is the coefficient. A smaller value of  $\varphi$  calculated by Eq. (9) indicates a better seismic-control effect. The functional recoverability and comfort requirements of structures are considered comprehensively. Then, each coefficient is determined as follows: for multiple occurring earthquakes,  $\alpha = 0.7$ ,  $\beta = \gamma = 0.2$ ,  $\mu = 0$ ; and for design, rare, and extremely rare earthquakes,  $\alpha = 0.5$ ,  $\beta = \gamma = \mu = 0.2^{53}$ . The calculation results of the objective function  $\varphi$  for each condition are shown in Table 8.

The results show that under the same level of earthquake ground motion, the seismic-control effect of the structure is in the order of SCFDF, SCDF, and BRBF, from best to worst. SCFDs can effectively reduce structural damage and enhance post-earthquake recovery. BRBs exhibit an excellent effect in controlling the PIDR of structures; however, residual deformations cannot be eliminated. Dampers based only on SMAs can also effectively reduce  $\theta_{\rm max}$  and  $\theta_{\rm r}$ ; however, their cost is high and they are unsuitable for practical engineering.

#### **Conclusions**

In this study, an improved multilinear constitutive model of SMAs that considers strength degradation and residual strain is proposed. Subsequently, the improved model was applied to a new type of self-centering damper, and a time-history analysis was conducted to investigate its structural control effect. Notable conclusions are summarized as follows:

- 1. The proposed SMA constitutive model, developed through secondary development on the OpenSees platform and incorporating residual deformation, strength degradation, and the separation of loading—unloading in the martensitic hardening stage, achieved high-fidelity hysteresis simulation. Key parameters (e.g., equivalent damping ratio) exhibited errors below 9% versus experimental data, with exceptional performance in low-strain scenarios (errors < 3% at 4% ~ 5% strains). This model can be integrated with Steel01 to simulate the mechanical behavior of self-centering friction energy-dissipating dampers, serving as a robust tool for subsequent elasto-plastic time-history analysis.
- 2. By establishing and comparatively analyzing a refined finite-element model of a reinforced concrete frame with self-centering friction dampers, BRB braces, and self-centering dampers under seismic action, the SCFD demonstrated superior performance: (a) it reduced residual inter-story drift ratios (RIDR) to below 0.1% under rare earthquakes, meeting FEMA P—58 repair—free standards; (b) it decreased peak inter-story drift ratios (PIDR) by 43.5% compared to uncontrolled structures under extremely rare earthquakes (PGA = 0.6g), preventing structural collapse.
- 3. A comprehensive performance index (Eq. 9) effectively ranked damper effectiveness (SCFD>SCDF>BRBF), providing a multi-criteria optimization tool for seismic design.

#### Limitations and future work

- 1. Current experimental validations were limited to specific damper sizes and seismic inputs; future studies should address multi-scale prototypes and near-fault pulse-type ground motions.
- 2. Economic analyses of SCFD manufacturing/installation costs and long-term durability under environmental corrosion require further investigation.
- 3. Integration of smart materials and digital twin technologies will be pursued to enable adaptive control and sustainable lifecycle management of SMA-based dampers.

#### Data availability

Some or all data, models, or code that support the findings of this study are available from the corresponding author upon reasonable request.

Received: 17 March 2025; Accepted: 19 June 2025

#### Published online: 01 July 2025

#### References

- 1. Zhai, Z. P., Guo, W., Yu, Z. W., He, C. J. & Zeng, Z. F. Experimental and numerical study of S-shaped steel plate damper for seismic resilient application. *Eng. Struct.* 221, 111006. https://doi.org/10.1016/j.engstruct.2020.111006 (2020).
- Qiu, C. X., Wang, H. Y., Liu, J. W., Qi, J. & Wang, Y. M. Experimental tests and finite element simulations of a new SMA-steel damper. Smart Mater. Struct. 29(3), 035016. https://doi.org/10.1088/1361-665X/ab6abd (2020).
- 3. Koutsoloukas, L., Nikitas, N. & Aristidou, P. Passive, semi-active, active and hybrid mass dampers: A literature review with associated applications on building-like structures. *Dev. Built. Environ.* 12, 100094. https://doi.org/10.1016/j.dibe.2022.100094 (2022)
- 4. Qi, Q. M. et al. Axial-flexure-shear model for seismic analysis of RC thin-walled hollow piers. Soil Dynam. Earthq. Eng. 195, 109375. https://doi.org/10.1016/j.soildyn.2025.109375 (2025).
- Wada, A., Qu, Z., Motoyui, S. & Sakata, H. Seismic retrofit of existing SRC frames using rocking walls and steel dampers. Front. Archit. Civ. Eng. China. 5(3), 259–266. https://doi.org/10.1007/s11709-011-0114-x (2011).
   Ferraioli, M., Laurenza, B., Lavino, A., Frattolillo, C. & Matteis, G. D. Seismic retrofit of a steel-reinforced concrete hospital
- Ferraioli, M., Laurenza, B., Lavino, A., Frattolillo, C. & Matteis, G. D. Seismic retrofit of a steel-reinforced concrete hospital building using continuous energy-dissipative steel columns. *Steel Compos. Struct.* 47(4), 467–488. https://doi.org/10.12989/scs.20 23.47.4.467 (2023).
- 7. Aghagholizadeh, M. & Makris, N. Seismic response of a yielding structure coupled with a rocking wall. Struct. Eng. 144(2), 04017196. https://doi.org/10.1061/(ASCE)ST.1943-541X.0001894 (2018).
- 8. Javidan, M. M., Naeem, A. & Kim, J. Seismic retrofit of structures using added steel column friction dampers. Steel Compos. Struct. 49, 257–270. https://doi.org/10.12989/scs.2023.49.3.257 (2023).
- 9. Yao, Z. C., Wang, W. & Zhu, Y. Z. Experimental evaluation and numerical simulation of low-yield-point steel shear panel dampers. Eng. Struct. 245, 112860. https://doi.org/10.1016/j.engstruct.2021.112860 (2021).
- 10. Ferraioli, M., Lavino, A. & Matteis, G. D. A design method for seismic retrofit of reinforced concrete frame buildings using aluminum shear panels. Arch. Civ. Mech. Eng. 23(2), 106. https://doi.org/10.1007/s43452-023-00639-1 (2023).
- 11. Javidan, M. M., Kim, J., Javidan, M. M. & Kim, J. An experimental study on a steel multi-slit damper for seismic retrofit of soft-first story structures. Steel Compos. Struct. 50(6), 721–734. https://doi.org/10.12989/scs.2024.50.6.721 (2022).
- 12. Javidan, M. M., Assefa, J. D. & Kim, J. Seismic retrofit of low-rise structures using rotational viscoelastic dampers. *Structures* 58, 105403. https://doi.org/10.1016/j.istruc.2023.105403 (2023).
- 13. Javidan, M. M., Ahmad, R. N., Park, S. & Kim, J. Seismic retrofit of structures using steel frames with viscoelastic hinges. *Structures* 64, 106585. https://doi.org/10.1016/j.istruc.2024.106585 (2024).
- 14. Song, G., Ma, N. & Li, H. N. Applications of shape memory alloys in civil structures. *Eng. Struct.* 28(9), 1266–1274. https://doi.org/10.1016/j.engstruct.2005.12.010 (2006).
- Rojob, H. & El-Hacha, R. Self-prestressing using Iron-SMA for flexural strengthening of reinforced concrete beams. ACI Struct. J. 114(2), 523-532. https://doi.org/10.14359/51689455 (2017).
- Dolce, M., Cardone, D. & Marnetto, R. Implementation and testing of passive control devices based on shape memory alloys. *Earthquake Engng Struct. Dyn.* 29(7), 945–968 (2000).
- 17. Qian, H., Li, H. & Song, G. B. Experimental investigations of building structure with a superelastic shape memory alloy friction damper subject to seismic loads. *Smart Mater. Struct.* 25(12), 125026. https://doi.org/10.1088/0964-1726/25/12/125026 (2016).
- 18. Silwal, B. & Ozbulut, O. E. Aftershock fragility assessment of steel moment frames with self-centering dampers. *Eng. Struct.* 168, 12–22. https://doi.org/10.1016/j.engstruct.2018.04.071 (2018).
- 19. Yang, C. W., DesRoches, R. & Leon, R. Design and analysis of braced frames with shape memory alloy and energy-absorbing hybrid devices. *Eng. Struct.* 32(2), 498–507. https://doi.org/10.1016/j.engstruct.2009.10.011 (2010).
- El-Feky, M. H. et al. Computer simulation for the seismic behavior of bridge expansion joints enhanced with SMA: Case study. Case Stud. Constr. Mater. 20(2024), e02782. https://doi.org/10.1016/j.cscm.2023.e02782 (2024).
- 21. Kim, Y. C., Lee, H. W. & Hu, J. W. Behavioral characteristics analysis of pretension damper with superelastic shape memory alloy. Case Stud. Constr. Mater. 20(2024), e03121. https://doi.org/10.1016/j.cscm.2024.e03121 (2024).
- Zhang, Y. F. & Zhu, S. Y. Seismic response control of building structures with superelastic shape memory alloy wire dampers. Eng. Mech. 134(3), 240–251. https://doi.org/10.1061/(ASCE)0733-9399(2008)134:3(240) (2008).
- 23. Casagrande, L., Menna, C., Asprone, D., Ferraioli, M. & Auricchio, F. Chapter 21 Buildings. in Shape Memory Alloy Engineering 2nd edn 689–729 (2021). https://doi.org/10.1016/B978-0-12-819264-1.00021-2.
- 24. Ferraioli, M., Concilio, A. & Molitierno, C. Seismic performance of a reinforced concrete building retrofitted with self-centering shape memory alloy braces. *Earthq. Eng. Vib.* 21(3), 785–809. https://doi.org/10.1007/s11803-022-2113-4 (2022).
- Shi, F., Ozbulut, O. E. & Zhou, Y. Influence of shape memory alloy brace design parameters on seismic performance of selfcentering steel frame buildings. Struct. Control. Health Monit. 27, 1–18. https://doi.org/10.1002/stc.2462 (2020).
- Gur, S., Mishra, S. K. & Chakraborty, S. Performance assessment of buildings isolated by shape-memory-alloy rubber bearing: Comparison with elastomeric bearing under near-fault earthquakes. Struct. Control Health Monit. 21(4), 449–465. https://doi.org/10.1002/stc.1576 (2014).
- 27. Hu, J. W. Seismic analysis and parametric study of SDOF lead-rubber bearing (LRB) isolation systems with recentering shape memory alloy (SMA) bending bars. *J. Mech. SCI TECHNOL* **30**(7), 2987–2999. https://doi.org/10.1007/s12206-016-0608-5 (2016).
- Naeem, A., Eldin, M. N., Kim, J. & Kim, J. Seismic performance evaluation of a structure retrofitted using steel slit dampers with shape memory alloy bars. Int. J. Steel Struct. 17(4), 1627–1638. https://doi.org/10.1007/s13296-017-1227-4 (2017).
- 29. Liu, M., Zhou, P. & Li, H. Novel self-centering negative stiffness damper based on combination of shape memory alloy and prepressed springs. *J. Aerosp. Eng.* 31(6), 04018100. https://doi.org/10.1061/(ASCE)AS.1943-5525.0000926 (2018).

- Ortin, J. & Planes, A. Thermodynamics of thermoelastic martensite transformations. ACTA Metal. Sin. 37(5), 1433–1441. https://doi.org/10.1016/0001-6160(89)90175-2 (1989).
- 31. Berveiller, M., Patoor, E. & Buisson, M. Thermomechanical constitutive equations for shape memory alloys. *Le Journal de Physique IV* 1(C4), 387–396. https://doi.org/10.1051/jp4:1991458 (1991).
- 32. Auricchio, F. & Sacco, E. Thermo-mechanical modelling of a superelastic shape-memory wire under cyclic stretching-bending loadings. *Int. J. Solids Struct.* 38(34–35), 6123–6145. https://doi.org/10.1016/S0020-7683(00)00282-1 (2001).
- 33. Sun, P. Q. & Hwang, K. Q. Micromechanics modeling for the constitutive behavior of ploycrystalline shape memory alloys-I Derivation of general relations. *J. Mech. Phys. Solids.* 1(41), 1–17. https://doi.org/10.1016/0022-5096(93)90060-S (1993).
- 34. Boyd, J. G. & Lagoudas, D. C. (1996), A thermodynamical constitutive model for shape memory materials. Part I. The monolithic shape memory alloy. *Int. J. Plascity* 12, 805–842. https://doi.org/10.1016/S0749-6419(96)00030-7 (1996).
- 35. Boyd, J. G. & Lagoudas, D. C. Thermomechanical response of shape memory composites. *J. Intel. Mat. Sys. Str.* 5(3), 333–346. https://doi.org/10.1177/1045389X9400500306 (1994).
- 36. Brinson, L. C. One-dimensinal constitutive behavior of shape memory alloys: Thermomechanical derivation with non-constant material functions and redefined material variable. *J. Intel. Mat. Sys. Str.* 4(2), 229–242. https://doi.org/10.1177/1045389 X9300400213 (1993).
- 37. Liang, C. & Rogers, C. A. One-dimensional thermomechanical constitutive relations for shape memory materials. *J. Intel. Mat. Sys. Str.* 8(4), 285–302. https://doi.org/10.1177/1045389X9000100205 (1990).
- Raniecki, B., Lexcellent, C. & Tanaka, K. Thermodynamic models of pseudoelastic behaviour of shape memory alloys. Arch. Mech. 44(3), 261–284 (1992).
- Tanaka, K. Phenomenological description of the mechanical behavior of shape memory alloys. *Jpn. Soc. Mech. Eng.* 53(491), 1368
  (1987)
- 40. H. Özdemir, Nonlinear transient dynamic analysis of yielding structures (University of California, California, Berkeley, 1976).
- Graesser, E. J. & Cozzarelli, F. A. Shape-memory alloys as new materials for aseismic isolation. J. Eng. Mech. 117(11), 2590–2608. https://doi.org/10.1061/(ASCE)0733-9399(1991)117:11(2590) (1991).
- 42. Graesser, E. J. & Cozzarelli, F. A. A proposed three-dimensional constitutive model for shape memory alloys. *J. Intel. Mat. Sys. Str.* 5(1), 78–89. https://doi.org/10.1177/1045389X9400500109 (1994).
- 43. Li, R., Chen, Q. F., Xu, Z. F. & Hu, B. Experimental study and modification of the constitutive model of superelastic SMA considering multi-factor effects. Case Stud. Constr. Mater. 17(2022), e01611. https://doi.org/10.1016/j.cscm.2022.e01611 (2022).
- 44. Lagoudas, D.C., Mayes, J.J., Khan, M.M. Simplified shape memory alloy (SMA) material model for vibration isolation. in Smart Structures and Materials 2001: Modeling, Signal Processing, and Control in Smart Structures. International Society for Optics and Photonics 4326(2001), 452–461 (2021).
- 45. Chang, Z. Q., Xing, G. H., Han, M. & Liu, B. Q. Multiparameter optimization design of self-centering friction damper using shape memory alloy bars. *J. Earthq. Eng.* 27(4), 833–851. https://doi.org/10.1080/13632469.2022.2033354 (2023).
- Han, M. et al. Seismic design optimization of frame structure with self-centering SMA friction damper. Eng. Mech. 40(7), 112–120. https://doi.org/10.6052/j.issn.1000-4750.2021.11.0912 (2023).
- 47. SolidWorks Premium 2020 SP0.0. SolidWorks Corporation. https://www.Solidworks.com.
- 48. Han, M., Chang, Z. Q., Xing, G. H., Peng, P. Z. & Liu, B. Q. Cyclic behavior and seismic control performance of SMA friction damper. Smart Mater. Struct. 32, 075010. https://doi.org/10.1088/1361-665X/acd91b (2023).
- 49. GB50011-2010 Code for Seismic Design of Buildings (China Architecture & Building Press, Beijing, 2010).
- 50. China Academy of Building Research. PKPM Structural Design Software User Manual. (China Architecture and Building Press, Beijing, 2023).
- Wang, Y. Research on Seismic Performance and Design Method of Buckling-restrained Brace and Brace-frame Structure, Ph.D. thesis (China University of Mining and Technology-Beijing, 2014).
- 52. Zhang, J. Seismic Behavior and Design Method of Reinforced Concrete Frames Retrofitted with Buckling-Restrained Braces, Ph.D. thesis (Harbin Institute of Technology, 2015).
- 53. Applied Technology Council, and National Earthquake Hazards Reduction Program (US) 2012 Seismic performance assessment of buildings (Federal Emergency Management Agency).
- 54. Qu, J. T. & Li, H. N. Optimum installation of viscoelastic dampers in structures. J. Vib. Shock 27(6), 87–91. https://doi.org/10.134 65/j.cnki.jvs.2008.06.032 (2008).

#### **Acknowledgements**

The authors gratefully acknowledge the financial support from the National Natural Science Foundation (No. 52308137), Natural Science Basic Research Program of Shaanxi (No.2023-JC-QN-0617), Key Research and Development Program of Shaanxi (2022LL-JB-13).

#### **Author contributions**

W.L.: Investigation. Z.C.: Supervision, Methodology. M.H.: Writing—original draft, Investigation. J.L.: Writing—original draft, Investigation. B.L.: Writing—review & editing, supervision. Q.J.: Methology, Conceptualization.

#### **Declarations**

#### Competing interests

The authors declare no competing interests.

#### Additional information

Correspondence and requests for materials should be addressed to Z.C.

Reprints and permissions information is available at www.nature.com/reprints.

**Publisher's note** Springer Nature remains neutral with regard to jurisdictional claims in published maps and institutional affiliations.

Open Access This article is licensed under a Creative Commons Attribution-NonCommercial-NoDerivatives 4.0 International License, which permits any non-commercial use, sharing, distribution and reproduction in any medium or format, as long as you give appropriate credit to the original author(s) and the source, provide a link to the Creative Commons licence, and indicate if you modified the licensed material. You do not have permission under this licence to share adapted material derived from this article or parts of it. The images or other third party material in this article are included in the article's Creative Commons licence, unless indicated otherwise in a credit line to the material. If material is not included in the article's Creative Commons licence and your intended use is not permitted by statutory regulation or exceeds the permitted use, you will need to obtain permission directly from the copyright holder. To view a copy of this licence, visit <a href="http://creativecommons.org/licenses/by-nc-nd/4.0/">http://creativecommons.org/licenses/by-nc-nd/4.0/</a>.

© The Author(s) 2025